ACS MATERIALS LETTERS

Cite This: ACS Materials Lett. 2019, 1, 418−424

www.acsmaterialslett.org

LETTER

# Development of Polyene-Bridged Hybrid Rhodamine Fluorophores for High-Resolution NIR-II Imaging

Yibing Shi, Wei Yuan, Qingyun Liu, Mengya Kong, Zhenhua Li, Wei Feng, Ke Hu,* and Fuyou Li*

Department of Chemistry & State Key Laboratory of Molecular Engineering of Polymers & Collaborative Innovation Center of Chemistry for Energy Materials, Fudan University, 220 Handan Road, Shanghai 200433, People's Republic of China

Supporting Information

**ABSTRACT:** **This work presents a polyene bridging strategy on Rhodamine-type dye analogues (Rh824, Rh926, and Rh1029) for tuning absorption and emission wavelengths from the first near-infrared window (NIR-I; 750−900 nm) to the unprecedented second near-infrared window (NIR-II; 1000−1700 nm). Phosphatidylcholine (PC) enclosures of the dyes improve water solubility and triple the fluorescent quantum yields. The representative NIR-II fluorophore Rh1029-PC presents significantly higher spatial resolution, compared to NIR-I fluorophore Rh824-PC, when performing in vivo vascular imaging. We construct a mouse vascular hemorrhage model and apply Rh1029-PC as the angiography agent in NIR-II window for the first time. The images show superior clarity of the hemorrhage positions in the NIR-II window, suggesting the successful application of the hybrid Rhodamine-derived dye in NIR-II fluorescent bioimaging.**

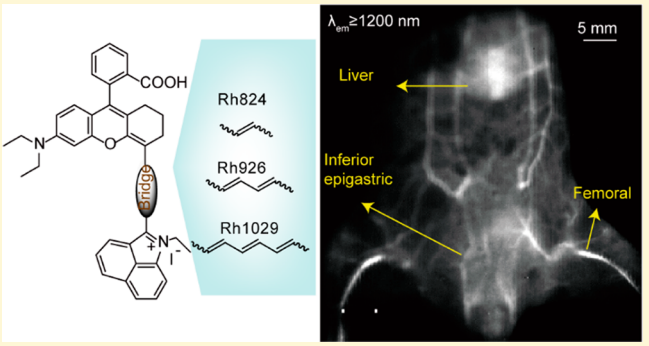


Fluorescent imaging as one of the bioimaging modalities in clinics has several unique advantages, including fast temporal resolution for real-time imaging, multichannel capability, and low cost.[1,2] Over decades of research, noninvasive fluorescent imaging technology has evolved to be a powerful tool for studying physiological functions, and providing guidance for precise surgery.[3] However, most of the fluorescent imaging studies in the literature focused on emission wavelengths from visible to near infrared range up to 900 nm (NIR-I). In this wavelength window, the imaging quality commonly suffered from shallow penetration depth (typically <3 mm) and low spatial resolution (typically 1−2 mm) due to strong tissue absorption, scattering, and autofluorescence.[4,5] To overcome these drawbacks, a growing number of studies have been focusing on fluorescent materials that emit at even longer wavelengths, that is, the second near-infrared (NIR-II) window from 1000 nm to 1700 nm.[3,6−9] Despite stronger absorption from water, excitation and emission of longer wavelengths cause both lower light scattering and autofluorescence intensities. Probing fluorescence signals in the NIR-II window provides potentially better spatial resolution than in the NIR-I (750−900 nm) window.[10]

In search of suitable fluorescent materials, quite a few NIR-II fluorophores were developed, including PbS or $Ag_2S$ quantum dots,[11] single-walled carbon nanotubes,[12,13] and nanoparticles containing luminescence down-converting rare-earth elements as a whole.[14−17] Many of these nanoparticle-type fluorescent materials indeed show superior imaging quality but still need to solve issues such as high toxicity and slow excretion for practical use.[7] Small organic molecules, on the other hand, have fewer of these types of concerns. Indocyanine Green (ICG) and Methylene Blue (MB), for instance, are two clinically safe fluorescent agents but are primarily used for imaging in the NIR-I window.[18−20] Therefore, the pursuit of highly fluorescent small organic fluorophores in the NIR-II window recently triggered great interest from researchers in the fluorescent imaging field. Donor−acceptor−donor (D-A-D) structures and extended $\pi$-conjugates are two general design principles to approach the goal.[21] For instance, Dai's group first demonstrated CH1055, which is a D-A-D molecule for targeted tumor imaging in the NIR-II window.[22,23] They achieved an in vivo imaging depth of ∼4 mm with superior spatial resolution and especially fast renal clearance. Zhang's group further improved spatial imaging resolution with an excitation wavelength in the NIR-II region by using a 1064-nm-laser excitable cyanine-type dye[6] or a flavylium heterocycle variant for multiplexed biosensing.[5,24]

Received: July 10, 2019
Accepted: August 29, 2019
Published: August 29, 2019






DOI: 10.1021/acsmaterialslett.9b00265
ACS Materials Lett. 2019, 1, 418−424

Rhodamine is a class of robust small organic fluorophores widely used in photochemistry studies such as dye laser medium or fluorescent labeling.[25] They have high quantum yields of emission and can sustain high power of laser irradiation. However, most Rhodamine dyes emit photons in the visible region upon excitation with small Stokes shifts. Much effort now has been devoted to hybrid Rhodamine variants, including metalloid xanthene rhodamines, pyronin rhodamines, hybrid cyanine-rhodamines, etc. for further bathochromic shift of fluorescent emission.[26−29] Nevertheless, NIR-II-emitting hybrid Rhodamine fluorophores are still rare. In this article, inspired by the notion of hybrid Rhodamine construction, we present a general approach of introducing a polyene bridge between the Rhodamine-type fluorophore and benz[c,d]indolium moiety for bathochromic shift toward further NIR windows (Scheme 1). The bridge consists of

**Scheme 1. Molecular Structures of Hybrid Rhodamine-benz[c,d]indolium Analogues with Variable Lengths of the Polyene Bridges**

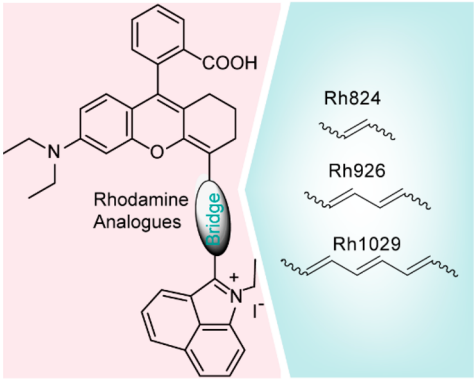


one to three repeating units of the vinylene group. Each vinylene extension is expected to red-shift the absorption spectrum by ∼100 nm.[27] We are able to tune the fluorophore in a systematic manner from NIR-I to NIR-II within the same molecular moiety. The tradeoff between the fluorescent quantum yield loss and the resolution gain from this conjugation bridge approach is closely examined in both of the NIR windows for mouse vascular imaging. In addition, we apply the hybrid Rhodamine series in a vascular hemorrhage model and elegantly demonstrate the advantage of decreased background scattering for sharp clarity in the NIR-II imaging window.

The synthetic routes to the polyene-bridged hybrid Rhodamine-benz[c,d]indolium analogues, Rh824, Rh926, and Rh1029 were presented in the Supporting Information (Figure S1).[28] Briefly, benz[c,d]indolium iodide (compound **I**) reacted with *N*,*N*′-diphenylformamide to form compound **II** and sequentially conjugated with compound **III** through condensation in acidic anhydride. The final product NIR-I dye Rh824 gave an overall yield of ∼50%. The yield was ∼41% for Rh926, based on similar synthetic procedures. However, the aforementioned synthetic sequence for Rh1029 only gave an overall yield of <10%. Diene-bridged cyanine-benz[c,d]-indolium dye was the major byproduct. We took a different approach for the synthesis of Rh1029. Prior to the introduction of **I**, we conducted condensation reaction between the anilines and **III**. In this way, the yield was improved to 30% for Rh1029.[30]

Figure 1 shows Vis-NIR absorption and fluorescent spectra of Rh824, Rh926, and Rh1029 in dichloromethane. The three

A

| Solvent :$CH_2Cl_2$ | Rh824 | Rh926 | Rh1029 |
|---|---|---|---|
| Abs Maxima (nm) | 824 | 926 | 1029 |
| Emission Maxima (nm) | 872 | 975 | 1093 |
| ε (×10⁴ L•mol⁻¹•cm⁻¹) | 5.28 | 3.05 | 1.9 |
| Φ (%) | 1.30 | 0.76 | 0.33 |

B

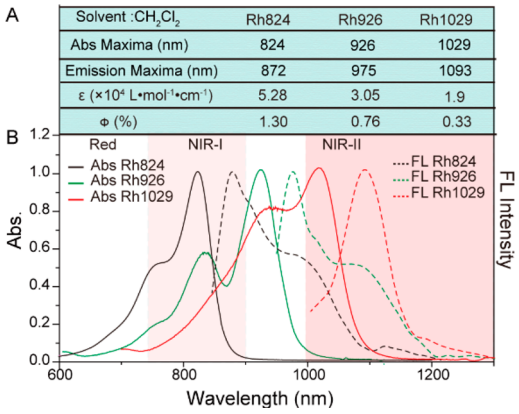


**Figure 1. (A) Photophysical properties of Rh824, Rh926, and Rh1029 in dichloromethane. (B) Normalized Vis-NIR absorption and fluorescence spectra of Rh824 (exc. 808 nm), Rh926 (exc. 915 nm), and Rh1029 (exc. 980 nm) in dichloromethane.**

fluorophores displayed absorption maxima at 824, 926, and 1029 nm with emissions peaked at 872, 975, and 1093 nm, respectively. The absorption maxima were ∼100 nm apart, which was in accordance with the increment of each vinylene bridge unit.[31] The existence of shoulder absorptions was possibly due to noncovalent dimerization of hybrid Rhodamine-based dyes.[32] Each fluorescent spectrum roughly mirrored the absorption and had a peak Stokes shift of ∼50−60 nm. The polyene bridges successfully moved emissions of the hybrid Rhodamine-benz[c,d]indolium analogues into biological transparent regions where Rh824 fell into the NIR-I window while Rh926 and Rh1029 appeared in the NIR-II region. We used commercially available IR1061 ($\Phi_{FL}$ = 0.53%) as the fluorescent actinometer[24,33,34] to obtain the relative quantum yields for these three dyes. The calculated quantum yields for Rh824, Rh926, and Rh1029 were 1.30%, 0.76%, and 0.33%, respectively. The increased flexibility and *cis*−*trans* isomerism caused a reduction in quantum yield (Φ) as the conjugated π-system was extended.[35] Detailed measurements and calculations are shown in Figure S2 in the Supporting Information.

The hybrid Rhodamine-benz[c,d]indolium analogues were hydrophobic in nature. We chose amphiphilic phosphatidylcholine (PC)[36] to solubilize the lipophilic molecules in water. Dyes would embed themselves into the multilayer phospholipids with the acidic tail anchored into assemblies of phospholipid acyl chains through hydrophobic−hydrophobic interaction.[37] The quantum yields of PC-enclosed dyes (Rh824-PC, Rh926-PC, and Rh1029-PC) were optimized by varying the synthesis temperature, dye:PC ratio, and reaction time. The optimal recipe contained a Rh1029:PC molar ratio of ∼1:5 (see Figure S3 in the Supporting Information). The quantum yields for Rh824-PC, Rh926-PC, and Rh1029-PC, based on this recipe, were 2.72%, 1.95%, and 1.27%, respectively (see Figure 2B, as well as Figure S4 in the Supporting Information), which tripled that of dyes dissolved in dichloromethane.[36] This increase in quantum yield could be due to space separation of fluorophores by hydrophobic alkyl chains of PC with literature precedence, but it is difficult to reach this conclusion definitively, based on the ground state



DOI: 10.1021/acsmaterialslett.9b00265
ACS Materials Lett. 2019, 1, 418−424

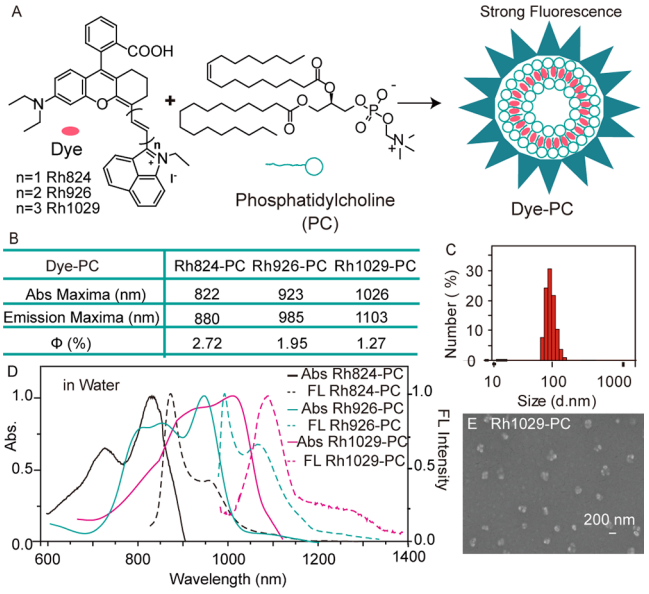


| Dye-PC | Rh824-PC | Rh926-PC | Rh1029-PC |
|---|---|---|---|
| Abs Maxima (nm) | 822 | 923 | 1026 |
| Emission Maxima (nm) | 880 | 985 | 1103 |
| Φ (%) | 2.72 | 1.95 | 1.27 |

**Figure 2. (A) Illustration of the enclosure of hybrid Rhodamine-benz[c,d]indolium analogues by phosphatidylcholine. (B) Photophysical properties of Rh824-PC, Rh926-PC, and Rh1029-PC in water. (C) Hydrodynamic size distribution of Rh1029-PC by dynamic light scattering. (D) Absorption and fluorescence spectra of Rh824 (10 μmol/L), Rh926-PC (20 μmol/L), and Rh1029-PC (35 μmol/L) in water. (E) SEM image of Rh1029-PC.**

electronic absorption, and this is subject to future investigations. The sizes of Rh1029-PC were ∼100 nm, on average, as determined by dynamic light scattering (DLS) (Figure 2C). We also tried other strategies, including PEGylation, embedding in silica or polystyrene (PS) matrix, or enclosure of bovine serum albumin (BSA) to solubilize the dyes in aqueous solutions. Nevertheless, PC was found to be the most efficient in improving the overall fluorescent quantum yields.

We further tested the photostability of the self-assembled nanovesicles by continuous laser illumination. The fluorescent emission of Rh1029-PC at 1100 nm and Rh824-PC at 880 nm remained unchanged after 1 h of illumination, suggesting excellent photostability. In stark contrast, FDA-approved ICG and ICG-PC suffered from a significant decrease of fluorescence measured at 835 nm in water (see Figure S5 in the Supporting Information). We selected Rh824-PC and Rh1029-PC in the following in vivo bioimaging and compared the imaging quality in the two NIR windows.

Prior to vascular bioimaging, we evaluated toxicity of Rh1029-PC based on cellular viability analysis in vitro. The cellular viability based on Hela cells was >86% for the 24-h group and >79% for the 48-h group (Figure S6 in the Supporting Information), which demonstrated low cytotoxicity of Rh1029-PC. In vivo vascular imaging was performed with nude mice intravenously injected with 1.0 mM of Rh824-PC or Rh1029-PC solution. The mice were then killed after 5 min and subjected to fluorescent signal collection on the NIR-I or NIR-II bioimaging apparatus. We sieved the optimal imaging region for vessel images of hindlimbs at a power density of 10 mW $cm^{-2}$. The NIR-II imaging apparatus was equipped with different longpass filters (1100, 1200, and 1300 nm longpasses) to collect different fluorescent wavelength regions. As shown in Figures 3A and 3C, the low signal-to-noise ratio of the capillary region in the NIR-I window using Rh824-PC frustrated accurate determination of the vascular width. In stark contrast, vascular images in the NIR-II window using Rh1029-PC were much sharper, thanks to much lower autofluorescent background noise. The Gaussian fit was conducted based on the luminescent intensity along the line drawn in the images.[1] The vascular width is 0.35 mm by using the full width at half maximum (FWHM) measure of a Gaussian peak fit ($\lambda_{em}\geq$ 1100 nm) in the femoral vascular region (Figure 3D1). The widths for the femoral vessel in the other two emission collection windows were calculated to be 0.31 mm ($\lambda_{em} \geq$ 1200 nm), and 0.27 mm ($\lambda_{em} \geq$ 1300 nm), respectively. We peeled off the skin of the nude mouse and measured the accurate width of the femoral vessel at the same position (Figure S7 in the Supporting Information). The vascular width was 0.30 mm, which was in accordance to the width obtained by data fitting in Figure 3D2. Therefore, the optimal imaging channel of $\lambda_{em}\geq$ 1200 nm region was selected as the best channel for in vivo bioimaging in this case. It maintained low autofluorescence and subtle image details at the same time. The resolution in this region was calculated to be 0.131 mm (see Figure S8 in the Supporting Information). Comparatively, the image in the $\lambda_{em}\geq$ 1100 nm region presented higher background interference and the image in the $\lambda_{em}\geq$ 1300 nm region missed part of capillaries, which were both inferior.

We calculated the vascular width (see Figures 3G and 3H) based on the calibration curve along the red dashed lines shown in Figures 3E and 3F. High autofluorescence in the NIR-I region caused difficulty in distinguishing the vascular signal curve, which inhibited imaging of subtle structures of vessels on the abdomen. In contrast, high-resolution imaging of vessels was achieved by Rh1029-PC, including parallel femoral artery and capillaries (Figure 3F). The vascular nest spread over the abdomen was distinguishable even near the liver region (see Figures 3F and 3H). Herein, Rh1029-PC exhibited images that are more precise with higher resolution and signal-to-noise value (SNR), compared to Rh824-PC in this case.

Vascular hemorrhage is a complication for multiple diseases, such as aneurysmal subarachnoid hemorrhage (aSAH),[38] skin necrosis,[39] and injuries caused by surgery and impact. As a result, clear and sharp images of vascular hemorrhage would help clinicians more accurately identify aSAH patients at risk and provide treatment more effectively.[28] With the superior spatial resolution of Rh1029-PC as a NIR-II fluorescent contrast agent, as demonstrated in the in vivo vascular imaging, we further applied this material in a mouse vascular hemorrhage model. We intravenously injected 300 μL Rh1029-PC (1 mM) at first. The left hindlimb of the nude mouse then was tied up for 10 min to cause a vascular hemorrhage. The right hindlimb remained untreated to provide a baseline of normal blood flow for comparison (see Figure 4A). Finally, the rope was released and both hindlimbs were imaged over a 1200 nm wavelength window shown side by side.

As shown in Figure 4B, to the naked eye, there was no macroscopic difference between the left and right hindlimbs. We highlighted the hemorrhage region using a green square and marked the fluorescent intensity as $I_{Hemorrhage}$. The corresponding hemorrhage-free region was highlighted by a blue square, and the fluorescent intensity in this region was marked as $I_{Hemorrhage\text{-}Free}$. The ratio value ($R$) reflecting the degree of hemorrhage accumulation was enclosed by a square with yellow dotted lines and calculated in Bruker molecular imaging software based on the formula below:


DOI: 10.1021/acsmaterialslett.9b00265
ACS Materials Lett. 2019, 1, 418−424

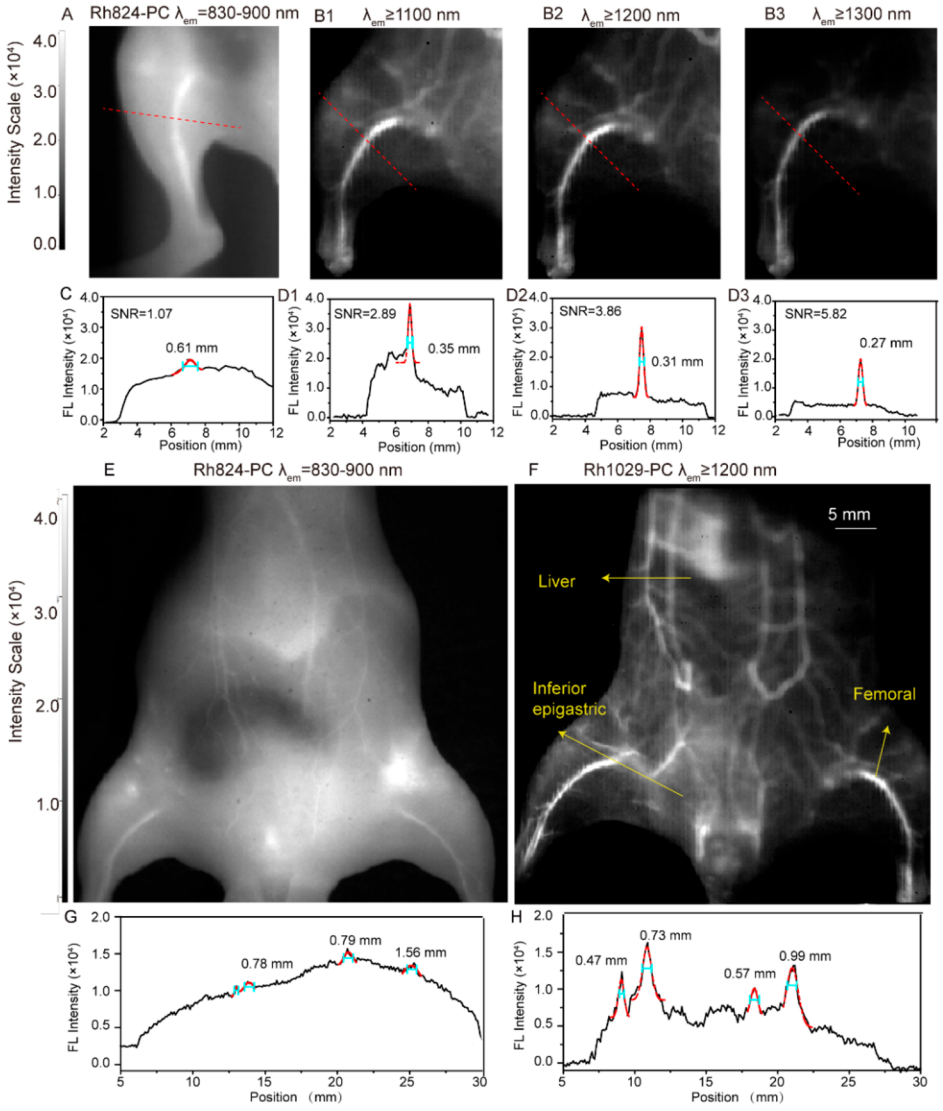


**Figure 3. Images of hindlimbs of nude mice intravenously injected with (A) Rh824-PC (1 mmol/L) under excitation of 808 nm laser (10 mW cm$^{-2}$) and (B) Rh1029-PC (1 mmol/L) (equipped with (B1) 1100 nm, (B2) 1200 nm, (B3) 1300 nm longpass filters, under excitation of a 980 nm laser (10 mW cm$^{-2}$) with the exposure time of 500 ms). (C) Corresponding fluorescent intensity along the red dashed line drawn in panel (A) and measured vascular width (blue line) to a Gaussian fit. (D1−D3) Corresponding fluorescent intensities along the red dashed lines in panels (B1−B3) and measured vascular widths (blue lines) to Gaussian fits. Images of abdomen of mice intravenously injected with (E) Rh824-PC (1 mmol/L) and (F) Rh1029-PC (1 mmol/L). (G, H) Corresponding fluorescent intensities along the red dashed lines of panels (E) and (F). The signal-to-noise ratios (SNR) values are the ratios of peak fluorescent intensity over average fluorescent noise intensity.**

$$R = \frac{I_{\text{Hemorrhage}} - I_{\text{Hemorrhage-Free}}}{I_{\text{Hemorrhage}}} \quad (1)$$

An $R$ value approaching unity would mean clear hemorrhage while a value of $R$ = 0 would indicate normal blood flow or hemorrhage-free tissues. We captured images of the left and right hindlimb at different delay times (0, 15, and 40 min). An image of the bound hindlimb is shown in Figure 4C1. Obviously, a huge portion of the hemorrhage formed in the left hindlimb. Some of the Rh1029-PC remained in femoral vessels and depicted the vascular shape, while most of it accumulated in the hemorrhage region and gave significant NIR-II fluorescent signals. The ratio (depicted in the inset of Figure 4C1) was generally ∼0.67−0.74. After removing the rope, the residual material Rh1029-PC in femoral vessels was back to vascular circulation. Since Rh1029-PC would accumulate in the liver upon blood circulation, the brightness of the vascular image for left hindlimb after removing the rope for 15 min (Figures 4C2 and 4D2) was diminished, compared to that in Figures 4C1 and 4D1. The ratio reflecting hemorrhage signal intensity spanned ∼0.69−0.82, which was possibly due to the increased accumulation of Rh1029-PC in the hemorrhage region through blood circulation. After 40 min, there was almost no signal remaining in the femoral vessels (see Figures 4C3 and 4D3). However, the ratio range increased even more and was ∼0.75−0.85. That being said, even after the material in the vessels was cleared up, Rh1029-PC still remained and helped to pinpoint the hemorrhage region due to blood leakage in the vicinity and ultraslow blood flow in that part.[40] Note that regions where $R$ was below zero might indicate a decreased blood volume caused by vascular clogs in hemorrhage areas.



DOI: 10.1021/acsmaterialslett.9b00265
ACS Materials Lett. 2019, 1, 418−424

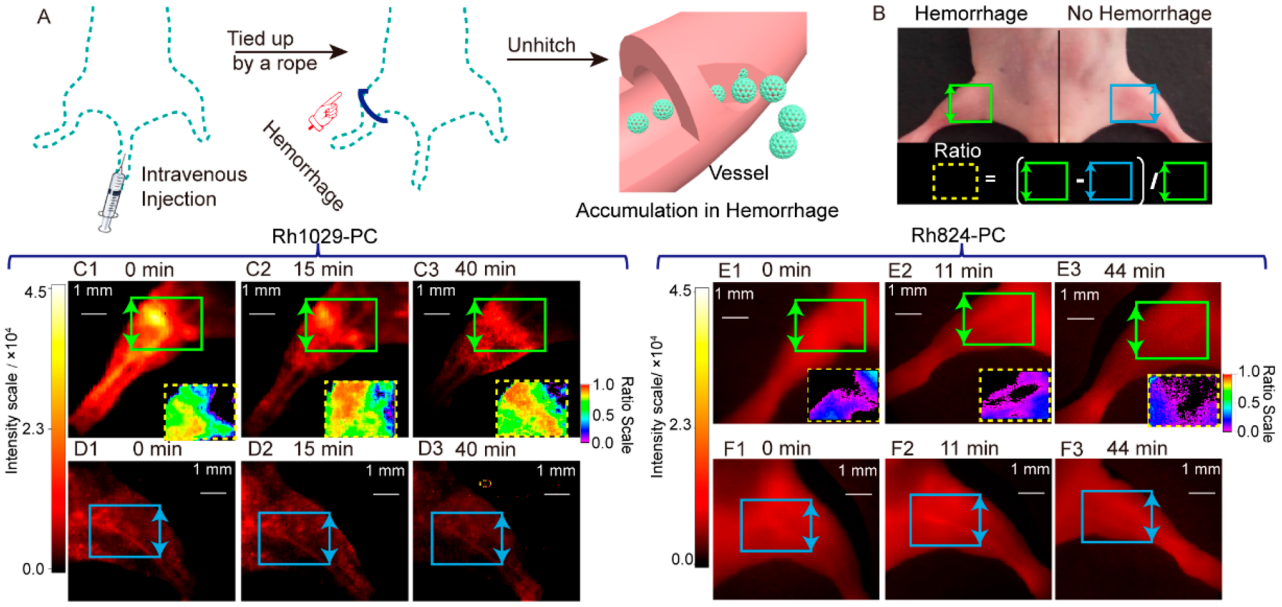


**Figure 4. (A) Illustration of procedures for vascular hemorrhage imaging experiments by Rh1029-PC and Rh824-PC, and (B) bright-field image of the nude mouse with rope to cause hemorrhage on the left hindlimb. The vascular hemorrhage region was bordered by the green square, the no-hemorrhage region was bordered by the blue square, and ratio value based on eq 1 is bordered by the yellow dotted square. (C) Images of left hindlimb and (D) right hindlimb from the nude mouse injected with Rh1029-PC: (C1−C3) after removing the rope that caused vascular hemorrhage from 0 to 40 min and (D1−D3) without treatment from 0 to 40 min. (E) Images of left hindlimb and (F) right hindlimb from the nude mouse injected with Rh824-PC: (E1−E3) after removing the rope that caused vascular hemorrhage from 0 to 44 min and (F1−F3) without treatment from 0 to 44 min. Insets in panels (C1−C3) show ratio values (*R*) that are based on the fluorescent intensity of Rh1029-PC at different times (0, 15, and 40 min). Insets in panels (E1)−(E3) show ratio values based on fluorescent intensity of Rh824-PC at different times (0, 11, and 44 min). The excitation source for Rh824-PC was an 808-nm laser equipped with an 880 ± 12 nm bandpass filter and that, for Rh1029-PC, was 980 nm laser with a 1200 nm longpass filter. Exposure time for both was 500 ms.**

NIR-I fluorophore Rh824-PC was also applied to vascular hemorrhage angiography, as a comparison to the NIR-II fluorophore with similar experimental conditions. However, the images were very blurry, probably because of strong background scattering, so much that vascular hemorrhage could hardly be identified. We highlighted the hitching region in the left hindlimb and symmetrical region in the right hindlimb and calculated the ratio in the same way. As shown in the inset in Figure 4E1, the calculated *R*-value was ∼0.11−0.24, which failed to diagnose the hemorrhage. After the rope was removed, images of the left and right hindlimbs were captured after 11 and 44 min, respectively. The value of *R* increased to 0.17−0.22 after 11 min, and 0.19−0.24 after 44 min (see Figures 4E2 and 4E3). Although Rh824-PC was expected to behave the same as Rh1029-PC, with regard to accumulating in the hemorrhage region, the low resolution in the NIR-I region caused difficulty in distinguishing the hemorrhage region both qualitatively and quantitatively.

In conclusion, we developed hybrid Rhodamine-benz[c,d]-indolium analogues (Rh824, Rh926, and Rh1029) with absorption peaks ranging from 824 nm to 1029 nm and emission peaks ranging from 872 nm to 1093 nm. The significant bathochromic shifts are attributed to the polyene bridges linking Rhodamine-type fluorophore and benz[c,d]-indolium. This molecular design can potentially expand the category of NIR fluorophores by modularly substituting the π-structure or the bridge for desired absorption or emission wavelengths. We demonstrated that phosphatidylcholine was a good vehicle for loading water-insoluble dyes such as Rh1029 and improved the fluorescent quantum yield. With good photostability and large Stokes shift, Rh1029-PC exhibited superior imaging quality in the NIR-II biological window. In vivo vascular imaging that revealed a comparison between Rh824-PC and Rh1029-PC showed advantages in imaging quality, in terms of high resolution and low background in NIR II. As an example of practical application, we constructed the vascular hemorrhage model and successfully pinpointed the area of hemorrhage using Rh1029-PC with preliminary imaging processing techniques. We believe that the molecular design approach that we developed for tuning wavelength of hybrid Rhodamine-based dyes would greatly expand new classes of NIR-II fluorophores. Our general fluorophore design strategy has opened an opportunity for well-studied versatile hybrid Rhodamine dyes to serve as robust fluorescent imaging agent in high-resolution in vivo bioimaging in the NIR-II window.

## ■ ASSOCIATED CONTENT

### Supporting Information

The Supporting Information is available free of charge on the ACS Publications website at DOI: 10.1021/acsmaterialslett.9b00265.

Experimental sections, detailed synthetic procedures, NMR spectra, Mass Spectra, quantum yield measurements, photostability measurements, cytotoxicity tests, additional imaging and vascular width measurement for peeled mice (PDF)

## ■ AUTHOR INFORMATION

### Corresponding Authors

*E-mail: khu@fudan.edu.cn (K. Hu).
*E-mail: fyli@fudan.edu.cn (F. Li).



DOI: 10.1021/acsmaterialslett.9b00265
*ACS Materials Lett.* 2019, 1, 418−424

**ORCID**

Wei Feng: 0000-0002-8096-2212

Ke Hu: 0000-0002-0240-7192

Fuyou Li: 0000-0001-8729-1979

### Author Contributions

F.L. and K.H. conceived the project and supervised the research. Y.S. performed the synthesis and was primarily responsible for conducting the experiments. W.Y., Q.L., and M.K. supported the bioimaging experiments. Z.L. supported the characterization of nanoparticles. Y.S., F.L., K.H., and W.F. analyzed the results, prepared the figures, and wrote the manuscript. All authors participated in the discussion and editing of the manuscript.

### Notes

The authors declare no competing financial interest.

## ■ ACKNOWLEDGMENTS

The authors thank the National Key R&D Program of China (Nos. 2016YFC1303100 and 2017YFA0205100), the National Natural Science Foundation of China (No. 21872037), the China Postdoctoral Science Foundation (Grant No. 2018M632006), and the National Postdoctoral Program for Innovative Talents (No. BX20190073) for financial support.

## ■ REFERENCES

(1) Antaris, A. L.; Chen, H.; Cheng, K.; Sun, Y.; Hong, G.; Qu, C.; Diao, S.; Deng, Z.; Hu, X.; Zhang, B.; Zhang, X.; Yaghi, O. K.; Alamparambil, Z. R.; Hong, X.; Cheng, Z.; Dai, H. A small-molecule dye for NIR-II imaging. *Nat. Mater.* **2016**, *15*, 235−242.

(2) Jaiswal, J. K.; Mattoussi, H.; Mauro, J. M.; Simon, S. M. Long-term multiple color imaging of live cells using quantum dot bioconjugates. *Nat. Biotechnol.* **2003**, *21*, 47−51.

(3) Vahrmeijer, A. L.; Hutteman, M.; van der Vorst, J. R.; van de Velde, C. J.; Frangioni, J. V. Image-guided cancer surgery using near-infrared fluorescence. *Nat. Rev. Clin. Oncol.* **2013**, *10*, 507−518.

(4) Hong, G.; Lee, J. C.; Robinson, J. T.; Raaz, U.; Xie, L.; Huang, N. F.; Cooke, J. P.; Dai, H. Multifunctional in vivo vascular imaging using near-infrared II fluorescence. *Nat. Med.* **2012**, *18*, 1841−1846.

(5) Lei, Z.; Sun, C.; Pei, P.; Wang, S.; Li, D.; Zhang, X.; Zhang, F. Stable, Wavelength-Tunable Fluorescent Dyes in the NIR-II Region for In Vivo High-Contrast Bioimaging and Multiplexed Biosensing. *Angew. Chem., Int. Ed.* **2019**, *58*, 8166−8171.

(6) Li, B.; Lu, L.; Zhao, M.; Lei, Z.; Zhang, F. An Efficient 1064 nm NIR-II Excitation Fluorescent Molecular Dye for Deep-Tissue High-Resolution Dynamic Bioimaging. *Angew. Chem., Int. Ed.* **2018**, *57*, 7483−7487.

(7) Yang, Q.; Ma, Z.; Wang, H.; Zhou, B.; Zhu, S.; Zhong, Y.; Wang, J.; Wan, H.; Antaris, A.; Ma, R.; Zhang, X.; Yang, J.; Zhang, X.; Sun, H.; Liu, W.; Liang, Y.; Dai, H. Rational Design of Molecular Fluorophores for Biological Imaging in the NIR-II Window. *Adv. Mater.* **2017**, *29*, 1605497.

(8) Smith, A. M.; Mancini, M. C.; Nie, S. Bioimaging: second window for in vivo imaging. *Nat. Nanotechnol.* **2009**, *4*, 710−711.

(9) He, S.; Song, J.; Qu, J.; Cheng, Z. Crucial breakthrough of second near-infrared biological window fluorophores: design and synthesis toward multimodal imaging and theranostics. *Chem. Soc. Rev.* **2018**, *47*, 4258−4278.

(10) Hemmer, E.; Benayas, A.; Légaré, F.; Vetrone, F. Exploiting the biological windows: current perspectives on fluorescent bioprobes emitting above 1000 nm. *Nanoscale Horiz* **2016**, *1*, 168−184.

(11) Hong, G.; Robinson, J. T.; Zhang, Y.; Diao, S.; Antaris, A. L.; Wang, Q.; Dai, H. In vivo fluorescence imaging with Ag2S quantum dots in the second near-infrared region. *Angew. Chem., Int. Ed.* **2012**, *51*, 9818−9821.

(12) Welsher, K.; Sherlock, S. P.; Dai, H. Deep-tissue anatomical imaging of mice using carbon nanotube fluorophores in the second near-infrared window. *Proc. Natl. Acad. Sci. U. S. A.* **2011**, *108*, 8943−8948.

(13) Diao, S.; Blackburn, J. L.; Hong, G.; Antaris, A. L.; Chang, J.; Wu, J. Z.; Zhang, B.; Cheng, K.; Kuo, C. J.; Dai, H. Fluorescence Imaging In Vivo at Wavelengths beyond 1500 nm. *Angew. Chem., Int. Ed.* **2015**, *54*, 14758−14762.

(14) Wang, R.; Li, X.; Zhou, L.; Zhang, F. Epitaxial seeded growth of rare-earth nanocrystals with efficient 800 nm near-infrared to 1525 nm short-wavelength infrared downconversion photoluminescence for in vivo bioimaging. *Angew. Chem., Int. Ed.* **2014**, *53*, 12086−12090.

(15) Ren, W.; Lin, G.; Clarke, C.; Zhou, J.; Jin, D. Optical Nanomaterials and Enabling Technologies for High-Security-Level Anticounterfeiting. *Adv. Mater.* **2019**, No. 1901430.

(16) Mi, C.; Zhou, J.; Wang, F.; Jin, D. Thermally enhanced NIR-NIR anti-Stokes emission in rare earth doped nanocrystals. *Nanoscale* **2019**, *11*, 12547−12552.

(17) Wen, S.; Zhou, J.; Zheng, K.; Bednarkiewicz, A.; Liu, X.; Jin, D. Advances in highly doped upconversion nanoparticles. *Nat. Commun.* **2018**, *9*, 2415.

(18) Ishizawa, T.; Saiura, A.; Kokudo, N. Clinical application of indocyanine green-fluorescence imaging during hepatectomy. *Hepatobiliary Surg. Nutr.* **2016**, *5*, 322−328.

(19) Starosolski, Z.; Bhavane, R.; Ghaghada, K. B.; Vasudevan, S. A.; Kaay, A.; Annapragada, A. Indocyanine green fluorescence in second near-infrared (NIR-II) window. *PLoS One* **2017**, *12*, No. e0187563.

(20) Carr, J. A.; Franke, D.; Caram, J. R.; Perkinson, C. F.; Saif, M.; Askoxylakis, V.; Datta, M.; Fukumura, D.; Jain, R. K.; Bawendi, M. G.; Bruns, O. T. Shortwave infrared fluorescence imaging with the clinically approved near-infrared dye indocyanine green. *Proc. Natl. Acad. Sci. U. S. A.* **2018**, *115*, 4465−4470.

(21) Yang, Y.; Zhao, Q.; Feng, W.; Li, F. Luminescent chemodosimeters for bioimaging. *Chem. Rev.* **2013**, *113*, 192−270.

(22) Antaris, A. L.; Chen, H.; Diao, S.; Ma, Z.; Zhang, Z.; Zhu, S.; Wang, J.; Lozano, A. X.; Fan, Q.; Chew, L.; Zhu, M.; Cheng, K.; Hong, X.; Dai, H.; Cheng, Z. A high quantum yield molecule-protein complex fluorophore for near-infrared II imaging. *Nat. Commun.* **2017**, *8*, 15269.

(23) Hong, G.; Antaris, A. L.; Dai, H. Near-infrared fluorophores for biomedical imaging. *Nat. Biomed. Eng.* **2017**, *1*, 1−22.

(24) Cosco, E. D.; Caram, J. R.; Bruns, O. T.; Franke, D.; Day, R. A.; Farr, E. P.; Bawendi, M. G.; Sletten, E. M. Flavylium Polymethine Fluorophores for Near- and Shortwave Infrared Imaging. *Angew. Chem., Int. Ed.* **2017**, *56*, 13126−13129.

(25) Yuan, L.; Lin, W.; Yang, Y.; Chen, H. A unique class of near-infrared functional fluorescent dyes with carboxylic-acid-modulated fluorescence ON/OFF switching: rational design, synthesis, optical properties, theoretical calculations, and applications for fluorescence imaging in living animals. *J. Am. Chem. Soc.* **2012**, *134*, 1200−1211.

(26) Tao, Z.; Hong, G.; Shinji, C.; Chen, C.; Diao, S.; Antaris, A. L.; Zhang, B.; Zou, Y.; Dai, H. Biological Imaging Using Nanoparticles of Small Organic Molecules with Fluorescence Emission at wavelengths Longer than 1000 nm. *Angew. Chem., Int. Ed.* **2013**, *52*, 13002−13006.

(27) Li, Z.; Mukhopadhyay, S.; Jang, S. H.; Bredas, J. L.; Jen, A. K. Supramolecular Assembly of Complementary Cyanine Salt J-Aggregates. *J. Am. Chem. Soc.* **2015**, *137*, 11920−11923.

(28) Su, Q.; Feng, W.; Yang, D.; Li, F. Resonance Energy Transfer in Upconversion Nanoplatforms for Selective Biodetection. *Acc. Chem. Res.* **2017**, *50*, 32−40.

(29) Wang, L.; Du, W.; Hu, Z.; Uvdal, K.; Li, L.; Huang, W. Hybrid Rhodamine Fluorophores in the Visible-NIR Region for Biological Imaging. *Angew. Chem., Int. Ed.* **2019**, *58*, 2−20.

(30) Sinha, S. H.; Owens, E. A.; Feng, Y.; Yang, Y.; Xie, Y.; Tu, Y.; Henary, M.; Zheng, Y. G. Synthesis and evaluation of carbocyanine dyes as PRMT inhibitors and imaging agents. *Eur. J. Med. Chem.* **2012**, *54*, 647−659.

(31) Yuan, L.; Lin, W.; Zheng, K.; He, L.; Huang, W. Far-red to near infrared analyte-responsive fluorescent probes based on organic fluorophore platforms for fluorescence imaging. *Chem. Soc. Rev.* **2013**, *42*, 622−661.



DOI: 10.1021/acsmaterialslett.9b00265
*ACS Materials Lett.* 2019, 1, 418−424

(32) Vickerstaff, T.; Lemin, D. R. Aggregation of Dyes in Aqueous Solution. *Nature* **1946**, *157*, 373.
(33) Hatami, S.; Würth, C.; Kaiser, M.; Leubner, S.; Gabriel, S.; Bahrig, L.; Lesnyak, V.; Pauli, J.; Gaponik, N.; Eychmüller, A.; Resch-Genger, U. Absolute photoluminescence quantum yields of IR26 and IR-emissive $Cd_{1-x}Hg_xTe$ and PbS quantum dots—method-and material-inherent challenges. *Nanoscale* **2015**, *7*, 133−143.
(34) Semonin, O. E.; Johnson, J. C.; Luther, J. M.; Midgett, A. G.; Nozik, A. J.; Beard, M. C. Absolute photoluminescence quantum yields of IR-26 dye, PbS, and PbSe quantum dots. *J. Phys. Chem. Lett.* **2010**, *1*, 2445−2450.
(35) Ballou, B.; Ernst, L. A.; Waggoner, A. S. Fluorescence Imaging of Tumors In Vivo. *Curr. Med. Chem.* **2005**, *12*, 795−895.
(36) Dubertret, B.; Skourides, P.; Norris, D. J.; Noireaux, V.; Brivanlou, A. H.; Libchaber, A. In Vivo Imaging of Quantum Dots Encapsulated in Phospholipid Micelles. *Science* **2002**, *298*, 1759−1762.
(37) Angelova, M. I.; Dimitrov, D. S. Liposome Electro formation. *Faraday Discuss. Chem. Soc.* **1986**, *81*, 303−311.
(38) Egashira, Y.; Xi, G.; Chaudhary, N.; Hua, Y.; Pandey, A. S. Acute Brain Injury after Subarachnoid Hemorrhage. *World Neurosurg* **2015**, *84*, 22−25.
(39) Wilkins, C. E. Extravasation injuries on regional neonatal units. *Arch. Dis. Child Fetal Neonatal. Ed.* **2004**, *89*, F274−F275.
(40) Zhang, X. D.; Wang, H.; Antaris, A. L.; Li, L.; Diao, S.; Ma, R.; Nguyen, A.; Hong, G.; Ma, Z.; Wang, J.; Zhu, S.; Castellano, J. M.; Wyss-Coray, T.; Liang, Y.; Luo, J.; Dai, H. Traumatic Brain Injury Imaging in the Second Near-Infrared Window with a Molecular Fluorophore. *Adv. Mater.* **2016**, *28*, 6872−6879.



DOI: 10.1021/acsmaterialslett.9b00265
*ACS Materials Lett.* 2019, 1, 418−424